Chapter 4

Imaging the Absorption Coefficient

Near infrared diffusing light probes offer new possibilities for medical imaging. Applications include non-invasive measurement of tissue oxygenation, and tumor detection and characterization [45]. Although investigators have determined the bulk optical properties based on a homogeneous model, direct imaging of the optical properties of heterogeneous tissue is an important potential improvement that has only recently been considered [46, 47]. It is expected that these images will lead to a more accurate representation of the optical properties for tissue characterization and functional imaging.

In this chapter we will assume that only the absorption coefficient varies with position. The other optical properties, such as the scattering coefficient, are assumed to be constant. To investigate the passage of photons through heterogeneous media we first write down the heterogeneous diffusion equation, and then generate solutions to this equation using two methods. The first involves a linear or Born expansion of the light energy density changes, and the second is an exponential or Rytov expansion of the light energy density changes.

We next discuss methods for inverting these solutions to obtain images of the medium. Again, we have investigated two different methods: the first is a matrix inversion, singular value decomposition (SVD), and the second is an algebraic reconstruction technique (SIRT). We present experimental results which demonstrate the feasibility of image reconstruction and characterization of the optical properties. Finally, we suggest an algorithm which exploits a high resolution imaging modality

such as MRI, x-ray tomography or ultra-sound to improve tissue characterization.

4.1   The Heterogeneous Diffusion Equation

The systems we are concerned with in this chapter have an absorption coefficient, $\mu_a(\mathbf{r})$ which may be divided into two components, the background, or homogeneous component, μ_a^o, and the spatially varying part $\delta\mu_a(\mathbf{r})$;

$$\mu_a(\mathbf{r}) = \mu_a^o + \delta\mu_a(\mathbf{r}). \tag{4.1}$$

When we substitute equation 4.1 into the diffusion equation or its related Helmholtz equation:

$$-D\nabla^2 U_{ac}(\mathbf{r}) + (-i\omega + v\mu_a)U(\mathbf{r}) = -A\delta(\mathbf{r}_s), \tag{4.2}$$

$$(\nabla^2 + k^2)U(\mathbf{r}) = A\delta(\mathbf{r}_s)/D. \tag{4.3}$$

we arrive at the heterogeneous equation for the light energy density at $\mathbf{r}$ from a source at $\mathbf{r}_s$, $A\delta(\mathbf{r}_s)$;

$$\left[\nabla^2 + k^2 + O(\mathbf{r})\right]U(\mathbf{r},\mathbf{r}_s) = A\delta(\mathbf{r}_s)/D, \tag{4.4}$$

$$O(\mathbf{r}) = v\delta\mu_a(\mathbf{r})/D. \tag{4.5}$$

To solve this heterogeneous diffusion equation, we will explore both the Born and the Rytov formulations. The following discussion is an adaptation of the discussion by Kak *et al.* [48].

4.2   Born Approximation

In the Born expansion we divide the photon density from a source at $\mathbf{r}_s$ measured at a position $\mathbf{r}$, into a linear superposition of its incident (homogeneous) and scattered (heterogeneous) parts;

$$U(\mathbf{r},\mathbf{r}_s) = U_o(\mathbf{r},\mathbf{r}_s) + U_{sc}(\mathbf{r},\mathbf{r}_s). \tag{4.6}$$

The heterogeneous diffusion equation (equation 4.4) becomes

$$\left[\nabla^2 + k^2 + O(\mathbf{r})\right]\left[U_o(\mathbf{r}, \mathbf{r}_s) + U_{sc}(\mathbf{r}, \mathbf{r}_s)\right] = -A\delta(\mathbf{r}_s)/D, \qquad (4.7)$$

If we subtract off the homogeneous Helmholtz equation,

$$(\nabla^2 + k^2)U_o(\mathbf{r}, \mathbf{r}_s) = -A\delta(\mathbf{r}_s)/D \qquad (4.8)$$

then we are left with the following heterogeneous Helmholtz equation for U_{sc}.

$$(\nabla^2 + k_0^2)U_{sc}(\mathbf{r}, \mathbf{r}_s) = -O(\mathbf{r})\left[U_o(\mathbf{r}, \mathbf{r}_s) + U_{sc}(\mathbf{r}, \mathbf{r}_s)\right] \qquad (4.9)$$

We next convolve this differential equation with the appropriate Green function solution to the Helmholtz equation, to arrive at the following integral solution for U_{sc};

$$U_{sc}(\mathbf{r}_d, \mathbf{r}_s) = -\int G(\mathbf{r} - \mathbf{r}_d)O(\mathbf{r})\left[U_o(\mathbf{r}, \mathbf{r}_s) + U_{sc}(\mathbf{r}, \mathbf{r}_s)\right] d^3r, \qquad (4.10)$$

$$G(\mathbf{r} - \mathbf{r}_d) = exp(ik|\mathbf{r} - \mathbf{r}_d|)/4\pi|\mathbf{r} - \mathbf{r}_d|. \qquad (4.11)$$

The integral is over the entire sample volume. We now make the Born approximation, i.e. we assume that

$$U_{sc}(\mathbf{r}) \ll U_o(\mathbf{r}), \qquad (4.12)$$

and we can write down an explicit solution for the scattered DPDW in a heterogeneous medium,

$$U_{sc}(\mathbf{r}_d, \mathbf{r}_s) = -\int G(\mathbf{r} - \mathbf{r}_d)O(\mathbf{r})U_o(\mathbf{r}, \mathbf{r}_s) \, d^3r \qquad (4.13)$$

with

$$U(\mathbf{r}_d, \mathbf{r}_s) = U_o(\mathbf{r}_d, \mathbf{r}_s) + U_{sc}(\mathbf{r}_d, \mathbf{r}_s) \qquad (4.14)$$

We will refer to this solution (equation 4.13) as the Born solution. Figure 4.1 demonstrates the components of the Born solution. One can think of this solution for U_{sc} as the number of photons which pass from the source ($\mathbf{r}_s$) to some position $\mathbf{r}$, scatter with an amplitude proportional to $\delta\mu_a$, and then travel from the position $\mathbf{r}$ to a detector at $\mathbf{r}_d$.
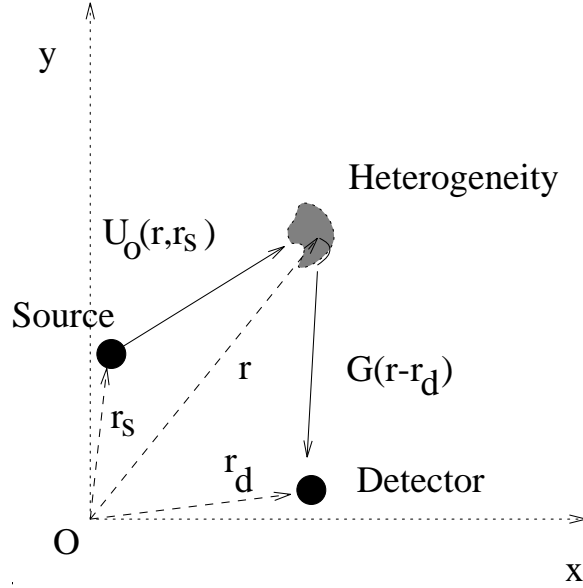
Figure 4.1: Schematic of the Born solution to the heterogeneous diffusion equation.

4.3   Rytov Approximation

In the Rytov expansion we again divide the photon density into its incident (homogeneous) and scattered (heterogeneous) parts;

$$U(\mathbf{r}, \mathbf{r}_s) = \exp(\phi_o(\mathbf{r}, \mathbf{r}_s) + \phi_{sc}(\mathbf{r}, \mathbf{r}_s)), \tag{4.15}$$

$$U_o(\mathbf{r}, \mathbf{r}_s) = \exp(\phi_o(\mathbf{r}, \mathbf{r}_s)). \tag{4.16}$$

When we plug this into the diffusion equation we obtain,

$$(\nabla^2 + k^2 + O(\mathbf{r})) \exp(\phi_o(\mathbf{r}, \mathbf{r}_s) + \phi_{sc}(\mathbf{r}, \mathbf{r}_s)) = -A\delta(\mathbf{r}_s)/D, \tag{4.17}$$

$$\nabla^2 \phi_o(\mathbf{r}, \mathbf{r}_s) + \nabla^2 \phi_{sc}(\mathbf{r}, \mathbf{r}_s) + (\nabla \phi_o(\mathbf{r}, \mathbf{r}_s))^2 + (\nabla \phi_{sc}(\mathbf{r}, \mathbf{r}_s))^2 + k_o^2 + O(\mathbf{r})$$

$$+2\nabla \phi_o(\mathbf{r}, \mathbf{r}_s) \cdot \nabla \phi_{sc}(\mathbf{r}, \mathbf{r}_s) = (\exp(-\phi_o(\mathbf{r}, \mathbf{r}_s) - \phi_{sc}(\mathbf{r}, \mathbf{r}_s)))A\delta(\mathbf{r}_s)/D. \tag{4.18}$$

It is clear that at the source position, the scattered signal is negligible compared to the delta function source signal, so we can write the right hand side of this equation as $\exp(-\phi_o(\mathbf{r}))A\delta(\mathbf{r}_s)/D$. We then rewrite the homogeneous equation as,

$$(\nabla^2 + k^2) \exp(\phi_o(\mathbf{r}, \mathbf{r}_s)) = A\delta(\mathbf{r}_s)/D \tag{4.19}$$

$$\nabla^2 \phi_o(\mathbf{r}, \mathbf{r}_s) + (\nabla \phi_o(\mathbf{r}, \mathbf{r}_s))^2 + k^2 = \exp(-\phi_o(\mathbf{r}, \mathbf{r}_s))A\delta(\mathbf{r}_s)/D. \tag{4.20}$$

When we subtract the homogeneous equation 4.20 from equation 4.18 we are left with

$$2\nabla\phi_o(\mathbf{r},\mathbf{r}_s)\phi_{sc}(\mathbf{r},\mathbf{r}_s) + \nabla^2\phi_{sc}(\mathbf{r},\mathbf{r}_s) = -(\nabla\phi_{sc}(\mathbf{r},\mathbf{r}_s))^2 - O(\mathbf{r}). \qquad (4.21)$$

We then linearize this equation by noticing that

$$\nabla^2(U_o(\mathbf{r},\mathbf{r}_s)\phi_{sc}(\mathbf{r},\mathbf{r}_s)) = \nabla\cdot(\nabla U_o(\mathbf{r},\mathbf{r}_s)\phi_{sc}(\mathbf{r},\mathbf{r}_s) + U_o(\mathbf{r},\mathbf{r}_s)\nabla\phi_{sc}(\mathbf{r},\mathbf{r}_s)) \quad (4.22)$$

$$= \nabla^2 U_o(\mathbf{r},\mathbf{r}_s)\phi_{sc}(\mathbf{r},\mathbf{r}_s) + 2\nabla U_o(\mathbf{r},\mathbf{r}_s)\cdot\nabla\phi_{sc}(\mathbf{r},\mathbf{r}_s) + U_o(\mathbf{r},\mathbf{r}_s)\nabla^2\phi_{sc}(\mathbf{r},\mathbf{r}_s)$$

and using the fact that $\nabla^2 U_o(\mathbf{r}) = -k^2 U_o(\mathbf{r})$ [49] we can rewrite equation 4.23 as

$$2\nabla U_o(\mathbf{r},\mathbf{r}_s)\cdot\nabla\phi_{sc}(\mathbf{r},\mathbf{r}_s) + U_o(\mathbf{r},\mathbf{r}_s)\nabla^2\phi_{sc}(\mathbf{r},\mathbf{r}_s) = \qquad (4.23)$$

$$\nabla^2(U_o(\mathbf{r},\mathbf{r}_s)\phi_{sc}(\mathbf{r},\mathbf{r}_s)) + k^2 U_o(\mathbf{r},\mathbf{r}_s)\phi_{sc}(\mathbf{r},\mathbf{r}_s).$$

Finally, we can plug this result into equation 4.21 to obtain

$$(\nabla^2 + k^2)U_o(\mathbf{r},\mathbf{r}_s)\phi_{sc}(\mathbf{r},\mathbf{r}_s) = -U_o(\mathbf{r},\mathbf{r}_s)((\nabla\phi_{sc}(\mathbf{r},\mathbf{r}_s))^2 + O(\mathbf{r})). \qquad (4.24)$$

Just as we did with the Born approximation, we convert this differential equation into an integral equation by convoluting with the Green function solution.

$$U_o(\mathbf{r}_d,\mathbf{r}_s)\phi_{sc}(\mathbf{r}_d,\mathbf{r}_s) = -\int G(\mathbf{r}-\mathbf{r}_d)U_o(\mathbf{r},\mathbf{r}_s)((\nabla\phi_{sc}(\mathbf{r},\mathbf{r}_s))^2 + O(\mathbf{r}))d^3r. \qquad (4.25)$$

We now make the Rytov approximation, $(\nabla\phi_{sc}(\mathbf{r},\mathbf{r}_s))^2 << O(\mathbf{r})$, and write the solution for the scattered phase as

$$\phi_{sc}(\mathbf{r}_d,\mathbf{r}_s) = -\frac{1}{U_o(\mathbf{r}_d,\mathbf{r}_s)}\int G(\mathbf{r}-\mathbf{r}_d)(v\delta\mu_a(\mathbf{r})/D)U_o(\mathbf{r},\mathbf{r}_s)d^3r. \qquad (4.26)$$

ϕ_{sc} will be referred to as the Rytov solution.

4.4 Breakdown of the Born and Rytov Approximations

Although the structure of the Born and Rytov solutions look very similar, there are some fundamental differences in their validity and use. We immediately see that the Born approximation makes the assumption that the scattered wave is small, and
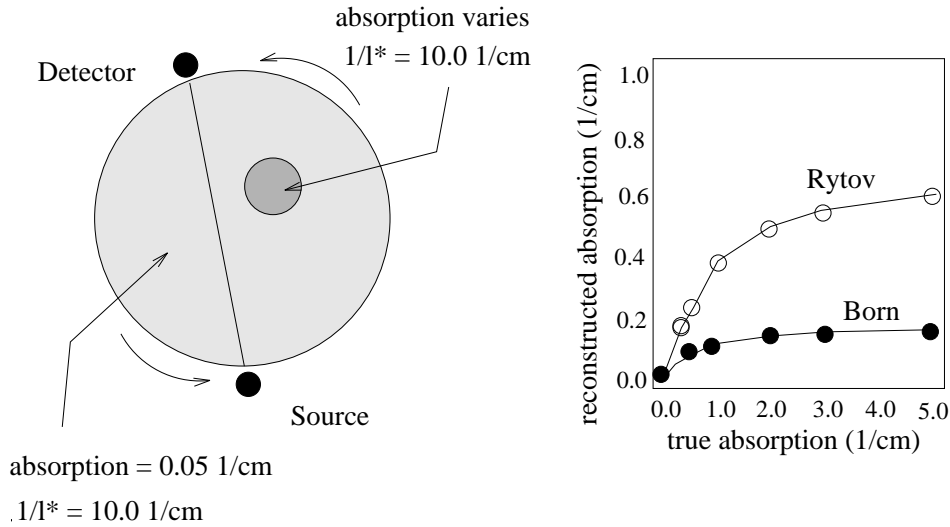
Figure 4.2: A comparison of the Born and Rytov approximations. A 1.0 cm diameter sphere is embedded in a medium with an absorption of 0.03 cm^{-1} and a reduced scattering coefficient of 10.0 cm^{-1}. Although a cylindrical region was reconstructed, an infinite model was used for both the forward and inverse problems.

the scattered wave scales approximately linearly with the absorption. In biological tissue we are interested in imaging absorption values which vary from about 0.02 cm^{-1} to 0.30 cm^{-1}. In fact, this linear assumption will break down for absorption differences greater than about 0.10 cm^{-1}, well within our region of interest. The Rytov approximation does not place a restriction on the magnitude of the scattered wave change, but rather assumes that the scattered field is slowly varying. Figure 4.2 demonstrates the breakdown of each approximation in the context of an isolated spherical heterogeneity. We see that the Rytov approximation is much more suitable for most biological situations. These and other differences will be discussed in section 4.8 and chapter 6.

4.5   Inverting the Solutions to the Heterogeneous Diffusion Equation

Our goal is to use either the Born or Rytov equations to solve for the absorption as a function of position within the medium. Thus we must invert the integral equations

(4.13, 4.26). There are many methods available to find the best solution to the inverse problem. But care must be taken since the integral equation is a Fredholm integral of the first kind (FI) and is highly susceptible to high frequency noise. A FI is an equation of the form

$$u(x) = \int_a^b k(x, s)\alpha(s)ds. \tag{4.27}$$

The difficulty in solving a FI for α arises from the instability of the inverse operator. Certain high frequency oscillatory noise in a solution may be screened out by the integral operator, giving a result which is very close to the left hand side. For example, if th correct solution to our problem is $\alpha(s)$, consider the residual of another solution $\alpha(s) + \delta\alpha(s)$ where

$$\delta\alpha(s) = \exp(i\omega s) \tag{4.28}$$

The residual, $\delta u(x)$ that this alternate solution adds to the measurements is

$$\delta u(x) = \int_a^b k(x, s)\delta\alpha(s)ds \tag{4.29}$$

$$= \int_a^b k(x, s)\exp(iws)ds. \tag{4.30}$$

If we integrate by parts,

$$\delta u(x) = \frac{1}{i\omega}k(x, s)\delta\alpha(s)\Big|_b^a - \frac{1}{i\omega}\int_a^b \frac{\partial k(x, s)}{\partial s}\exp(iws)ds \tag{4.31}$$

we see that the residual is of order $1/\omega$. Thus high frequency solutions for α will contribute little to the measurement, but can contribute significantly to the the image.

There are regularization schemes, such as Tikhonov regularization, which reduce the effect of high frequency noise on the reconstructed image. To invert the following equation;

$$\vec{u} = \tilde{A}\vec{x} \tag{4.32}$$

we would minimize the norm

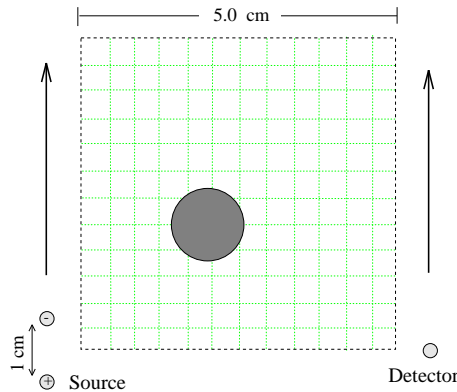$$||\vec{u} - \tilde{A}\vec{x}||. \tag{4.33}$$

Figure 4.3: A typical scanning geometry and volume digitization.

To use Tikhonov regularization, we minimize the equation

$$||\vec{u} - \tilde{A}\vec{x}|| + \beta||\vec{x}|| \tag{4.34}$$

where β is a free parameter which controls the level of regularization. Each time we try a different value of β. we create a new matrix to invert. Since inverting a matrix is computationally intensive, choosing the best value for β can be a time consuming process.

To invert our problem, we break up the region of interest into discrete volume elements and likewise digitize the integral equation to create a series of linear equations. A typical digitized volume and scattering geometry is shown in figure 4.3. We next solve these equations using two different techniques: (1) a regularized matrix inversion using singular value decomposition (SVD) and analysis and (2) an algebraic technique called simultaneous iterative technique (SIRT) with constraints.

In this work we have chosen to break the region into rectangular volume elements (voxels), but other geometries have also been investigated [17]. When choosing the voxel size, we must balance computation time with the desired resolution. Since our resolution is generally limited to about 0.5 cm [22], we typically choose to use voxels with approximately 0.2 cm edges. Once the space has been digitized into N voxels, the integral equation is similarly digitized,

Born:

$$U_{sc}(r_{si}, r_{di}) = \sum_{j=1}^{N} G(r_j - r_{di}) O(r_j) U_o(r_{si}, r_j) h^3, \tag{4.35}$$

Rytov:

$$\phi_{sc}(r_{si}, r_{di}) = -\sum_{j=1}^{N} G(r_j - r_{di}) O(r_j) U_o(r_{si}, r_j) h^3 / U_o(r_{si}, r_{di}). \tag{4.36}$$

Here $\mathbf{r}_{si}$ ($\mathbf{r}_{di}$) is the ith source (detector), and h^3 is the volume of the voxel. The effect of this digitization has been studied by Patterson and Pogue [50]. A series of measurements of the amplitude and phase of the DPDW for different source-detector configurations yields a set of coupled, linear equations which relate the real and imaginary parts of the measurements to the values of $\delta\mu_a$ in the various voxels within the sample.

Born:

$$\begin{pmatrix} U_{sc}(\mathbf{r}_{s1}, \mathbf{r}_{d1}) \\ \vdots \\ U_{sc}(\mathbf{r}_{sm}, \mathbf{r}_{dm}) \end{pmatrix} = \begin{pmatrix} W_{11}^B & \cdots & W_{1n}^B \\ \vdots & \ddots & \vdots \\ W_{m1}^B & \cdots & W_{mn}^B \end{pmatrix} \begin{pmatrix} \delta\mu_a(\mathbf{r}_1) \\ \vdots \\ \delta\mu_a(\mathbf{r}_n) \end{pmatrix}$$

$$W_{ij}^B = G(r_{di}, r_j) U_o(r_{si}, r_j) v h^3 / D \tag{4.37}$$

Rytov:

$$\begin{pmatrix} \phi_{sc}(\mathbf{r}_{s1}, \mathbf{r}_{d1}) \\ \vdots \\ \phi_{sc}(\mathbf{r}_{sm}, \mathbf{r}_{dm}) \end{pmatrix} = \begin{pmatrix} W_{11}^R & \cdots & W_{1n}^R \\ \vdots & \ddots & \vdots \\ W_{m1}^R & \cdots & W_{mn}^R \end{pmatrix} \begin{pmatrix} \delta\mu_a(\mathbf{r}_1) \\ \vdots \\ \delta\mu_a(\mathbf{r}_n) \end{pmatrix}$$

$$W_{ij}^R = G(r_{di}, r_j) U_o(r_j, r_{si}) v h^3 / (U_o(r_{di}, r_{si}) D \tag{4.38}$$

W^B and W^R are referred to as the weights. The weights are a description of the relative importance of each voxel to a particular measurement. Recall that the measurements and weights are complex. Before we try to invert the problem, we rewrite the matrix as a real matrix;

Born:

$$
\begin{pmatrix}
\Re[U_{sc}(\mathbf{r}_{s1}, \mathbf{r}_{d1})] \\
\vdots \\
\Re[U_{sc}(\mathbf{r}_{sm}, \mathbf{r}_{dm})] \\
\Im[U_{sc}(\mathbf{r}_{s1}, \mathbf{r}_{d1})] \\
\vdots \\
\Im[U_{sc}(\mathbf{r}_{sm}, \mathbf{r}_{dm})]
\end{pmatrix}
=
\begin{pmatrix}
\Re[W_{11}^B] & \dots & \Re[W_{1n}^B] \\
\vdots & \ddots & \vdots \\
\Re[W_{m1}^B] & \dots & \Re[W_{mn}^B] \\
\Im[W_{11}^B] & \dots & \Im[W_{1n}^B] \\
\vdots & \ddots & \vdots \\
\Im[W_{m1}^B] & \dots & \Im[W_{mn}^B]
\end{pmatrix}
\begin{pmatrix}
\delta\mu_a(\mathbf{r}_1) \\
\vdots \\
\delta\mu_a(\mathbf{r}_n)
\end{pmatrix}
$$

$$
W_{ij}^B = \quad G(r_{di}, r_j)U_o(r_{si}, r_j)vh^3/D \tag{4.39}
$$

Rytov:

$$
\begin{pmatrix}
\Re[\phi_{sc}(\mathbf{r}_{s1}, \mathbf{r}_{d1})] \\
\vdots \\
\Re[\phi_{sc}(\mathbf{r}_{sm}, \mathbf{r}_{dm})] \\
\Im[\phi_{sc}(\mathbf{r}_{s1}, \mathbf{r}_{d1})] \\
\vdots \\
\Im[\phi_{sc}(\mathbf{r}_{sm}, \mathbf{r}_{dm})]
\end{pmatrix}
=
\begin{pmatrix}
\Re[W_{11}^R] & \dots & \Re[W_{1n}^R] \\
\vdots & \ddots & \vdots \\
\Re[W_{m1}^R] & \dots & \Re[W_{mn}^R] \\
\Im[W_{11}^R] & \dots & \Im[W_{1n}^R] \\
\vdots & \ddots & \vdots \\
\Im[W_{m1}^R] & \dots & \Im[W_{mn}^R]
\end{pmatrix}
\begin{pmatrix}
\delta\mu_a(\mathbf{r}_1) \\
\vdots \\
\delta\mu_a(\mathbf{r}_n)
\end{pmatrix}
$$

$$
W_{ij}^R = \quad G(r_{di}, r_j)U_o(r_j, r_{si})vh^3/(U_o(r_{di}, r_{si})D \tag{4.40}
$$

4.6   Singular Value Decomposition

We used two different methods to solve the inverse problem. The first is a direct matrix inversion method called singular value decomposition (SVD). This discussion of SVD has been adapted from *Numerical Recipes* [51].

Singular value decomposition is a powerful technique for solving singular, or nearly singular matrices. (See appendix A for a brief review of singular matrices.) It is based on a theorem of linear algebra which states:

Any MxN matrix **A**, whose number of rows M, is greater than or equal to its number of columns N, can be written as the product of an MxN column-orthogonal matrix **U**, an NxN diagonal matrix **W**, with positive or zero elements, and the transpose of an NxN orthogonal matrix **V**.

i.e.

$$
\begin{pmatrix} A \end{pmatrix} = \begin{pmatrix} U \end{pmatrix} \cdot \begin{pmatrix} w_1 & & & \\ & w_2 & & \\ & & \ddots & \\ & & & w_N \end{pmatrix} \cdot \begin{pmatrix} V^T \end{pmatrix}
$$

$$(M \ \times \ N) \qquad (M \ \times \ N) \cdot (\quad N \ \times \ N \quad) \cdot (N \ \times \ N) \qquad (4.41)$$

The matrices **U** and **V** are orthogonal in the sense that their columns are orthonormal,

$$\mathbf{U^T} \cdot \mathbf{U} = \mathbf{V^T} \cdot \mathbf{V} = \mathbf{1}. \tag{4.42}$$

and since **V** is square,

$$\mathbf{V} \cdot \mathbf{V^T} = \mathbf{1}. \tag{4.43}$$

We will not go into the details of how this matrix decomposition is achieved, but rather refer to reader to Forsythe *et al.* [52] for a complete description. If **A** is a square matrix, then **U** is a NxN matrix, and $\mathbf{U}^{-1} = \mathbf{U}^T$. In this case, the inverse of **A** is

$$
\begin{aligned}
\mathbf{A} &= \mathbf{U} \cdot diag(w_j) \cdot \mathbf{V^T}, & (4.44) \\
\mathbf{A^{-1}} &= (\mathbf{V^T})^{-1} \cdot diag(w_j)^{-1} \cdot \mathbf{U^{-1}}, & (4.45) \\
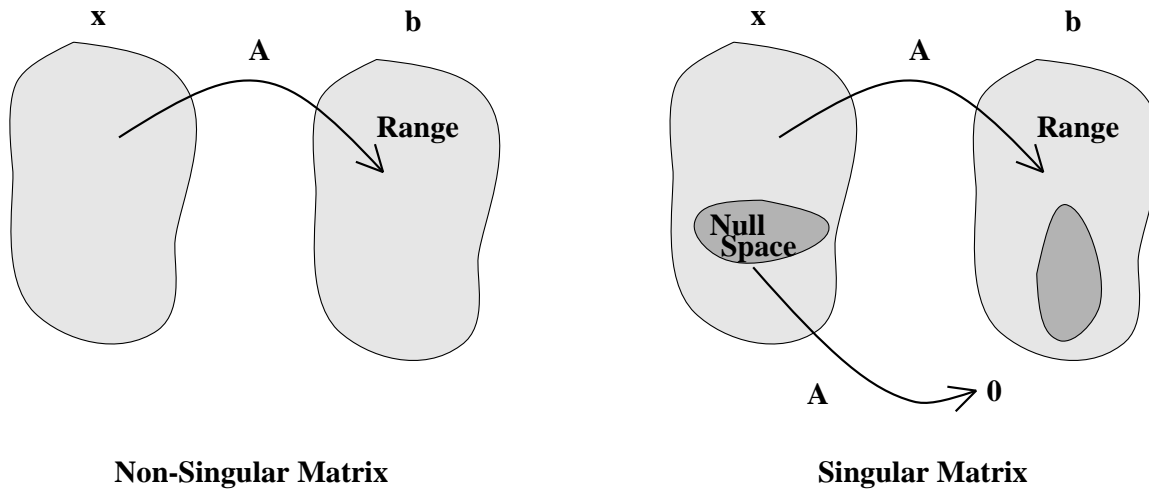\mathbf{A^{-1}} &= \mathbf{V} \cdot diag(1/w_j) \cdot \mathbf{U^T}. & (4.46)
\end{aligned}
$$

Figure 4.4: Linear algebra definitions for SVD

If the matrix **A** is non-singular, then calculation of the inverse is straightforward. However, if **A** is singular, or nearly singular, then the inverse is not well defined. However SVD can still give a solution. To understand the meaning of the SVD solution in this case, we must review some linear algebra definitions. Recall we are trying to solve the following matrix equation,

$$\mathbf{A} \cdot \mathbf{x} = \mathbf{b}. \tag{4.47}$$

A is a linear mapping from the vector space **x** to the vector space **b** as shown in figure 4.4. The subspace of **b** which can be reached by **x** is called the *range*. If **A** is singular, then there is some part of **x** that maps to zero, i.e.

$$\mathbf{A} \cdot \mathbf{x} = \mathbf{0} \tag{4.48}$$

This subspace of **x** is called the *null space*.

If the matrix **A** is non-singular, then there is no null space, and we will obtain a unique solution for $\mathbf{A}^{-1}$. If the matrix is singular the solution is not unique, but rather some combination of a general solution with linear combinations of the null space. Mathematically, each singularity corresponds to an eigenvalue (w_j) equal to zero. This creates a problem in the inverse when we try to compute $1/w_j$. We can

however, generate the solution with the smallest absorption by setting $1/w_j$ equal to zero when w_j equals zero. This is equivalent to throwing out all null space solutions. This altering of the eigenvalues is called singular value analysis (SVA). One of the powerful advantages of SVD is that the columns of $\mathbf{V}$ with zero eigenvalues form a basis set for the null space. Thus we can easily check the solutions that we are discarding for physical relevance.

The condition number of a matrix is the ratio of the smallest eigenvalue to the largest. The closer to unity the condition number, the more robust the inversion. A condition number of 10^{-6} for floating point precision of 10^{-12} for double precision will result in eigenvalues which are dominated by round off error. So SVA is also needed when the range of the eigenvalues is larger that the numerical precision of the computer. In the photon diffusion problem the condition number of the matrix is typically 10^{-12}. In this case we could zero the inverse of the small eigenvalues to generate the solution. We have found the that reconstructed images are improved when we use a simple smoothing algorithm [53] instead of eliminating the small eigenvalues;

$$w_j \quad \rightarrow \quad w_j + \sigma/w_j \tag{4.49}$$

$$\frac{1}{w_j} \quad \rightarrow \quad \frac{1}{w_j + \sigma/w_j} \tag{4.50}$$

Figure 4.5 demonstrates how the eigenvalues are effected by such an algorithm. σ is an arbitrary free parameter. If σ is much larger than the square of the maximum eigenvalue, then the eigenvalues are dramatically reduced, and we obtain a solution composed of only a few of the largest eigenfunctions. If σ is small compared to the square of the smallest eigenvalue, then there is effectively no smoothing, and we obtain a solution dominated by noise. Although the norm of the solution is reduced as we increase the smoothing, this is not the same as Tikhonov regularization where we minimize the norm of the residual plus the norm of the solution. The advantage of using the smoothing method over Tikhonov regularization is that we only have to perform the time consuming matrix decomposition once.

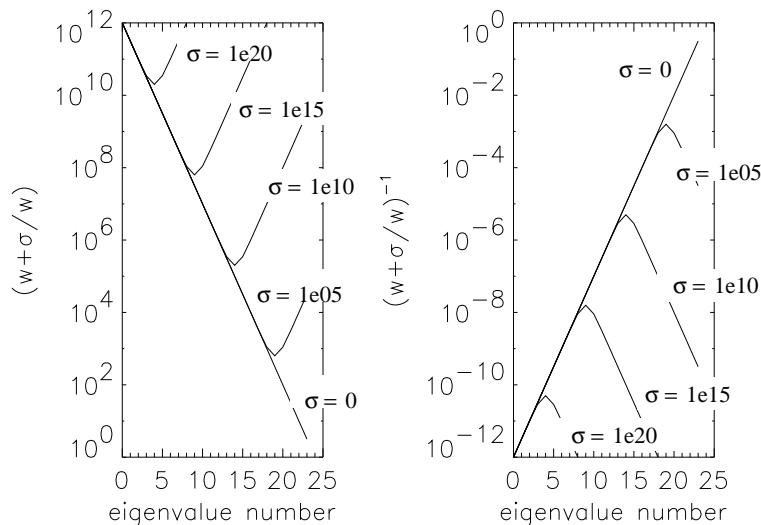We can now write down an explicit solution for the absorption as a function of

Figure 4.5: A singular or numerically singular matrix will have eigenvalues w_j which are zero or below the numerical precision of the calculation. In this case, we apply an eigenvalue smoothing procedure to minimize the effect of the small eigenvalues. The left panel shows how the eigenvalues are altered when $w_j \rightarrow w_j + \sigma/w_j$ for a series of different values of σ. The right panel shows how the inverse eigenvalue is affected.

position;

$$(\delta\mu_a) = [(V) \cdot (diag(\tfrac{1}{w_j+\sigma/w_j})) \cdot (U^T)] \cdot (data) \qquad (4.51)$$

As we increase σ, the image becomes less noisy and the image appears smoother. Since the smoothing algorithm always decreases the inverse of w_j, the reconstructed absorption will also decrease as the smoothing factor is increased.

There are many other regularization algorithms. In particular, Arridge *et al.* [19] have tested discussed Tikhonov regulation and SVA within the framework of diffusion imaging.

We have presented SVD for a square matrix. In our case, we often have many more voxels of unknown absorption than we do measurements. This means that we have more unknowns than equations. In this situation, we simply pad the matrix **A** with rows of zeros, and likewise pad the measurement vector with zeros. We can then invert the square matrix. The solution that we obtain will have a zero eigenvalue for each row of padding, and the solution we get is approximately the minimum

absorption solution as discussed above.

4.7   Algebraic Reconstruction Techniques

The second method we used to solve the linear system of equations is an algebraic reconstruction technique called SIRT - simultaneous iterative reconstruction technique. SIRT is a slight modification to an algebraic reconstruction technique (ART). In this section we will describe ART, and then SIRT. This discussion is based on the discussion in Kak *et al.* [48].

The ART algorithm is best demonstrated pictorially using a simple example. Suppose we have a system with two linear equations and two unknowns,

$$\tilde{\mathbf{A}} \cdot \vec{\mathbf{x}} = \vec{\mathbf{b}} \tag{4.52}$$

$$A_{11}x_1 + A_{12}x_2 = b_1 \tag{4.53}$$

$$A_{21}x_1 + A_{22}x_2 = b_2. \tag{4.54}$$

Here b_1 and b_2 are measurements, x_1 and x_2 are unknowns, and the A's are calculable. The solution space is a 2 dimensional space, i.e. a plane spanned by x_1 and x_2. The measurements are lines in that plane with slopes $-A_{11}/A_{12}$, $-A_{21}/A_{22}$ and intercepts $b_1/A_{12}, b_2/A_{22}$ as shown in figure 4.6a. The solution we are searching for is the intersection of these two lines. To find the intersection using ART, we first start from any point in space. (Typically we choose the origin as the initial guess.) We then move from the origin to the closest point on line first line as shown in figure 4.6. The mathematical equation for the move is

$$\vec{x}_{new} = \vec{x} - \frac{\vec{x} \cdot \vec{A} - b_j}{\vec{A} \cdot \vec{A}} \vec{A} \tag{4.55}$$

Here $\vec{A} = (A_{j1}, A_{j2}...A_{jN})$ and $\vec{x} = (x_1, x_2)$ is the the initial guess. We next make a similar move from the first line to the second line. These two moves constitute one iteration. This process, called the Kaczmarz method, is repeated until convergence is achieved. Tanube [54] has shown that the algorithm will always converge on the correct solution if a unique solution exists.
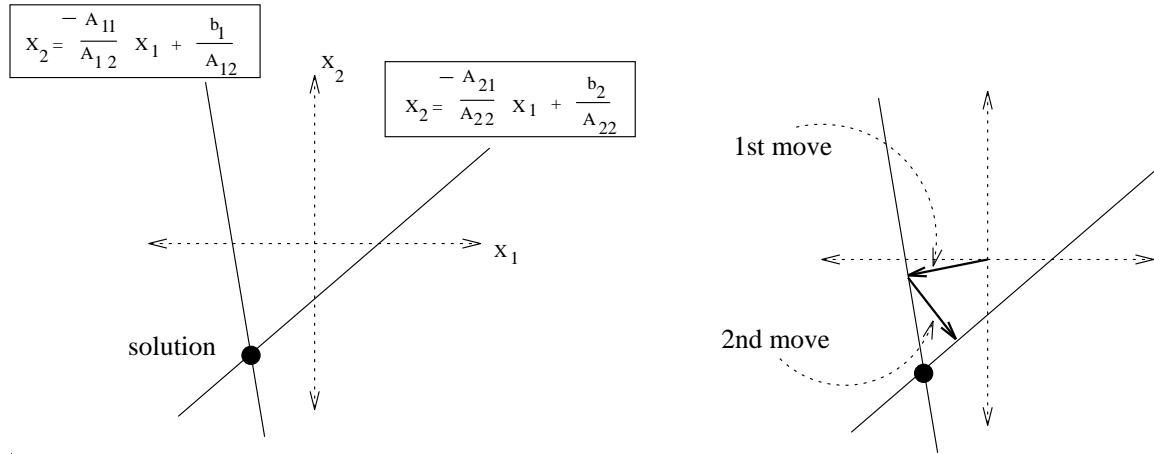
Figure 4.6: A graphical description of the algebraic reconstruction technique. In the left panel, the solid lines show the equations to be solved. In the right panel the thick arrows show the path that the algorithm takes as it moves from the initial guess, the origin, towards the correct solution. One iteration is shown.

Now suppose we add noise to the data. For the system of two equations and two unknowns, ART converges on the noisy solution as shown in figure 4.7a. If there are more equations than unknowns as shown in figure 4.7b, then no unique solution exists and the final solution oscillates in the neighborhood of the correct solution. If there are fewer equations than unknowns, then the process converges to a space (in this case a line) which contains the correct solution.

We have employed a slight modification to ART, called the simultaneous iterative reconstruction technique (SIRT). In SIRT we choose a starting point, and move from that starting point to the first line to find a new solution. We then move *from the starting point* to the second line. The two solutions are then averaged. SIRT is believed to produce better images than ART, at the expense of slightly slower convergence [48].

One of the major advantages of using the algebraic techniques instead of the matrix inversion is that the algebraic techniques allow the use of hard constraints. For example, we know that the reconstructed absorption should always be greater than zero. Thus at the end of each SIRT iteration, we zero any voxel which has a
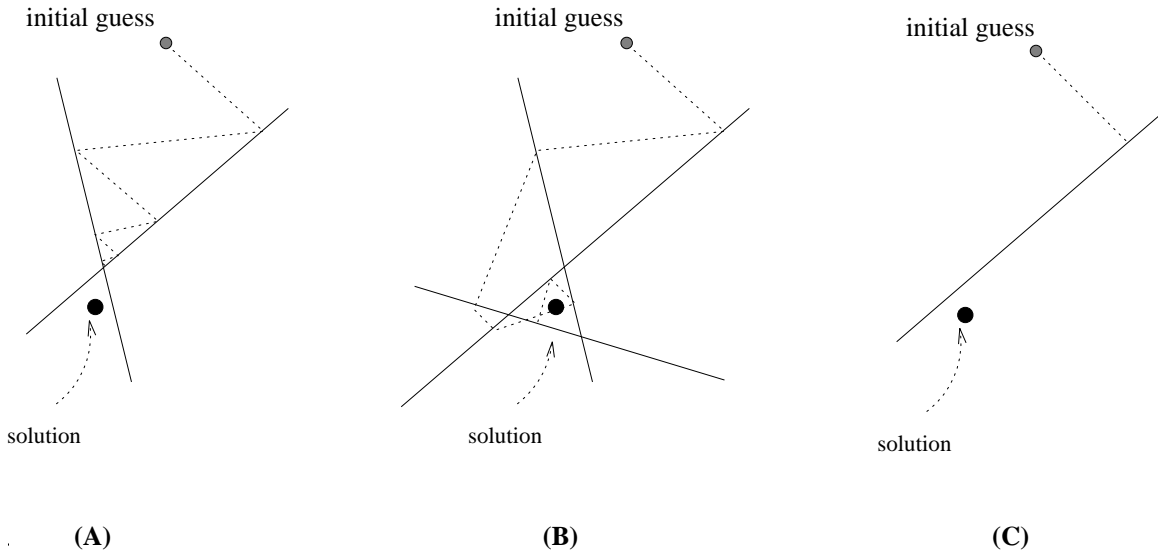
initial guess

initial guess

initial guess

solution

solution

solution

(A)   **(B)**   **(C)**

Figure 4.7: (A) ART with two noisy equations and two unknowns. (B) ART with more equations that unknowns (C) ART with fewer equations than unknowns.

negative absorption. Unless otherwise noted, we use this positivity constraint in all of our SIRT reconstructions.

When ART or SIRT is applied to photon diffusion imaging, we are searching for a solution in a N dimensional space, where N is the number of voxels. We are typically working in the case where the data is noisy, and we have fewer equations that unknowns. In our reconstructions we choose the smallest absorption solution by beginning our search at the origin. However in the cases where we have some *a priori* information, we can speed up the convergence, and arrive at a better solution by using this information to construct a good initial guess. Just as in SVD we had to choose a good smoothing parameter, in ART or SIRT, we have to decide when to stop the iterations. Ideally, the iterations should be stopped when the theoretical prediction coincides with the measured data within the experimental error. However, our situation is slightly more complicated than this.

In all of our simulations we have found that as we continue to iterate, the image of a sphere gets gradually smaller and more absorbing. Boas *et al.* [22] have demonstrated that even in a best case scenario, the difference between a small, highly absorbing
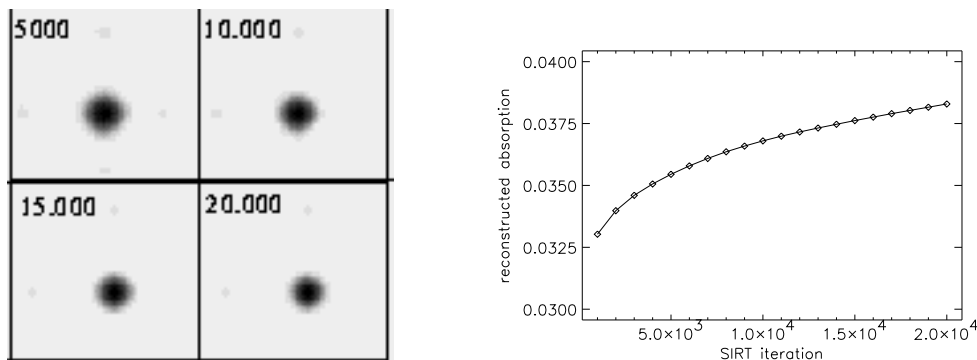
Figure 4.8: Left: The reconstructed images of an object at the center. Images are shown for 5,10,15 and 20 thousand SIRT iterations. Right: The reconstructed absorption (maximum value) as a function of iteration.

object and a larger, less absorbing object is practically immeasurable for objects with a diameter of less than 1 cm [22]. The authors demonstrated that there is a family of degenerate solutions which all conserve the quantity $\delta\mu_a v$ where v in the volume of the sphere. Thus, in the SIRT reconstructions, the consecutive iterations move the reconstruction through this family of solutions. Because we always start from the same initial guess (a homogeneous system) the reconstruction always moves through the family of solutions in the same way. Figure 4.8 demonstrates a series of reconstructions for different numbers of iterations. Note that as the number of iterations increases, the absorption of the object increases, and the size decreases. We have left the iteration number as a free parameter in our reconstructions.

4.8   Data Analysis

At this point, we must consider the measured data. In the Born approximation, we measure a voltage proportional to the total diffuse photon density at a particular position,

$$Voltage = C(U_o + U_{sc}), \tag{4.56}$$

In order to use the inverse solution (which was for a source of unit amplitude) we must eliminate the constant, C, and the homogeneous DPDW, U_o. C is a complex

number which includes such factors as the signal amplification, the efficiency of the light detection and the initial amplitude and phase of the source. In our experiments we measure the amplitude and phase of C by making measurements in a homogeneous infinite medium.

After calculating C, we have to subtract off the homogeneous part of the signal. This may be done using an analytic solution if the background properties are known. Alternatively, researchers have measured the signal with and without the presence on an inhomogeneity to eliminate the background. However, since both of these measurements are impractical in a clinical situation, we have instead chosen to make a reference measurement which does not rely on finding a homogeneous portion of the sample. In such a scheme we make two measurements with the same source and detector separations as shown in figure 4.9. We then subtract the two measurements, eliminating the homogeneous signal, and are left with only the difference of the heterogeneous signals.

$$Voltage\ 1 - Voltage\ 2 \quad = \quad C(U_o + U_{sc}^1) - C(U_o + U_{sc}^2) \qquad (4.57)$$

$$= \quad C(U_{sc}^1 - U_{sc}^2.) \qquad (4.58)$$

Of course using pairs of measurements changes the form of the weights;

$$W_{ij}^B = [G(r_j - r_{di1})U_o(r_{si1}, r_j) - G(r_j - r_{di2})U_o(r_{si2}, r_j)]\, vh^3/D. \qquad (4.59)$$

For the Rytov approximation, the situation is slightly simpler. In this case we measure

$$Voltage = CU_o \exp(\phi_{sc}) \qquad (4.60)$$

Again, we could measure or calculate C and U_o. However, if we use the reference scheme discussed above, and this time divide the two measurements,

$$ln\left(\frac{Voltage\ 1}{Voltage\ 2}\right) = ln\left(\frac{CU_o \exp(\phi_{sc1})}{CU_o \exp(\phi_{sc2})}\right) = \phi_{sc1} - \phi_{sc2}, \qquad (4.61)$$

Sources   Sources   Source

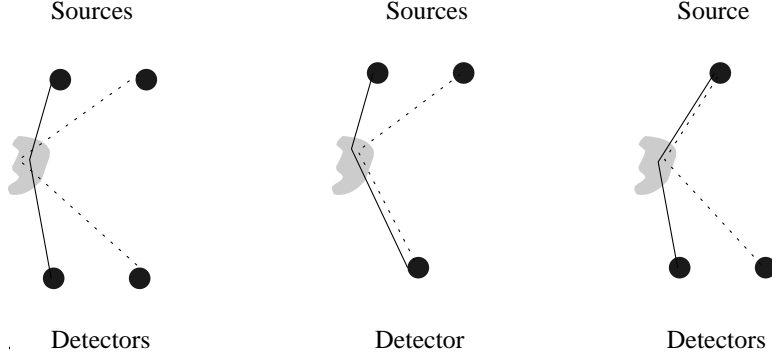Detectors   Detector   Detectors

Figure 4.9: Sample geometries for the reference measurements. See text for discussion.

we have eliminated the need to calibrate the machine to find C. The weights for this measurement pair are

$$
W_{ij}^R = \left(\frac{G(r_j - r_{di1})U_o(r_{si1}, r_j)}{U_o(r_{si1}, r_{di1})} - \frac{G(r_j - r_{di2})U_o(r_{si2}, r_j)}{U_o(r_{si2}, r_{di2})} \right) v h^3 / D. \qquad (4.62)
$$

Although we have eliminated the need to explicitly remove the background signal, we still need to know the background optical properties to calculate the weights. Specifically, U_o and G are functions of the background optical properties. If we incorrectly guess the background properties, then we introduce and error in G and U_o. For example, if we incorrectly guess the background absorption,

$$
G(\mathbf{r}) \quad \rightarrow \quad G(\mathbf{r}) + \frac{\partial G(\mathbf{r})}{\partial \mu_a} \Delta \mu_a + ... \rightarrow \left(1 + \frac{i|\mathbf{r}|}{2kD} \Delta \mu_a \right) G(\mathbf{r}) \qquad (4.63)
$$

$$
U_o(\mathbf{r}) \quad \rightarrow \quad U_o(\mathbf{r}) + \frac{\partial U_o(\mathbf{r})}{\partial \mu_a} \Delta \mu_a + ... \rightarrow \left(1 + \frac{i|\mathbf{r}|}{2kD} \Delta \mu_a \right) U_o(\mathbf{r}) \qquad (4.64)
$$

These errors show up in the weights for both the single source and double source weight functions, i.e. for a single source

$$
U_{sc}(\mathbf{r}_d, \mathbf{r}_s) \;\; = \;\; \int d^3 r (1 + \underbrace{\gamma(\mathbf{r}_d - \mathbf{r}) + \gamma(\mathbf{r} - \mathbf{r}_s) + O(\Delta \mu_a^2)}_{error}) G(\mathbf{r}_d - \mathbf{r}) U_o(\mathbf{r}, \mathbf{r}_s) h^3 / D,
$$

$$
\gamma(\mathbf{r}) \;\; = \;\; \frac{i|\mathbf{r}|\Delta \mu_a}{2kD} \qquad (4.65)
$$

and for the source pair,

$$
U_{sc}(\mathbf{r}_d, \mathbf{r}_{s1}) - U_{sc}(\mathbf{r}_d, \mathbf{r}_{s2}) = \qquad (4.66)
$$

$$\int d^3r \left[(1 + \underbrace{\gamma(\mathbf{r}_d - \mathbf{r}) + \gamma(\mathbf{r} - \mathbf{r}_{s1}) + O(\Delta\mu_a^2)}_{error})G(\mathbf{r}_d - \mathbf{r})U_o(\mathbf{r}, \mathbf{r}_{s1}) \right.$$

$$\left. - (1 + \underbrace{\gamma(\mathbf{r}_d - \mathbf{r}) + \gamma(\mathbf{r} - \mathbf{r}_{s2}) + O(\Delta\mu_a^2)}_{error})G(\mathbf{r}_d - \mathbf{r})U_o(\mathbf{r}, \mathbf{r}_{s2}) \right] h^3/D$$

We can see that the same *systematic* error is introduced in each equation for incorrect estimates of μ_a. If we now look at the calculation of U_{sc} from the measured data, we see the difference between the one source and two source measurements. When we measure the amplitude and phase, we measure the total wave,

$$U_{total} = U_o + U_{sc} \rightarrow U_{sc} = U_{total} - U_o. \tag{4.67}$$

In the one source Born approximation we must subtract off the calculated value of U_o. Since we use a guess for the background properties to calculate U_o, we introduce some error here, i.e.

$$U_{sc}(\mathbf{r}_s, \mathbf{r}_d) = U_{total}(\mathbf{r}_s, \mathbf{r}_d) - (1 + \gamma(\mathbf{r}_s, \mathbf{r}_d))U_o(\mathbf{r}_s, \mathbf{r}_d). \tag{4.68}$$

But when we use the two source referencing method, since $|\mathbf{r}_d - \mathbf{r}_{s1}| = |\mathbf{r}_d - \mathbf{r}_{s2}|$ this error is eliminated,

$$U_{sc}(\mathbf{r}_{s1}, \mathbf{r}_d) - U_{sc}(\mathbf{r}_{s2}, \mathbf{r}_d) = [U_{total}(\mathbf{r}_{s1}, \mathbf{r}_d) - (1 - \gamma(\mathbf{r}_d, \mathbf{r}_{s1}))(U_o(\mathbf{r}_{s1}, \mathbf{r}_d)] \tag{4.69}$$

$$- [U_{total}(\mathbf{r}_{s2}, \mathbf{r}_d) - (1 - \gamma(\mathbf{r}_d, \mathbf{r}_{s2}))U_o(\mathbf{r}_{s2}, \mathbf{r}_d)]$$

$$= U_{total}(\mathbf{r}_{s1}, \mathbf{r}_d) - U_{total}(\mathbf{r}_{s2}, \mathbf{r}_d) \tag{4.70}$$

There is no systematic error introduced in the measurement of U_{sc} when using the referencing scheme. Note that the if there is random measurement noise, then the subtraction of the two source measurements will effectively double the random noise.

Only the error in the processed data is reduced by the referencing scheme, the error in the weights is not reduced. Nevertheless, we have found that the procedure gives superior reconstruction as shown in figure 4.10. In these simulations, the background medium has an absorption coefficient of $\mu_a = 0.03$ cm^{-1} and a reduced

scattering coefficient of $\mu'_s = 10.0$ cm^{-1}. A 1 cm diameter sphere with the same reduced scattering coefficient as the background and an absorption coefficient of 0.05 cm^{-1} is embedded in the medium. The source (or sources) are scanned around the edges of a 7 cm square, and 26 measurements of amplitude and phase are simulated at a source modulation frequency of 500 MHz. We use the analytic solution for a sphere [10] to simulate the data. No noise was added to the data. We obtained data for two different configurations, first, a single source directly across from a single detector, and second, a source pair separated by 1 cm, directly across from a single detector.

Before we began reconstructing the image, we took a guess at the background absorption, (we assume that we know the correct reduced scattering coefficient). For the single source measurements, we use this guess to calculate the weights. We also use the guess to analytically subtract off the background signal from the total measurement. When the guess for the background was too low, (top left images in figure 4.10) a noisy image with a large positive absorption region in the center, and negative absorption region at the edges. When the background absorption is guessed correctly, we obtain a good image (center left image in figure 4.10), and when the background absorption guess is too high, we obtain the opposite image we saw when we under estimated the background absorption (lower left images in figure 4.10).

When we use the source pair, and underestimate the background absorption, this error cancels in the measured data, and the error is propagated only through the weights. In this situation, we can still see the outline of the solution in each case (see figure 4.11, right column). Although the error in the weights has effected the image quality, but it has not totally degraded the image.

When a positivity constraint is placed on the absorption solution (i.e. we set all voxels with negative absorption equal to zero in the reconstruction algorithm), the quality of the two source reconstructions is improved. The single source reconstruction only works when have the correct guess for the background (see figure 4.11).

If the geometry of the system does not allow these symmetric measurements, this algorithm for background subtraction cannot be used. Instead, the background
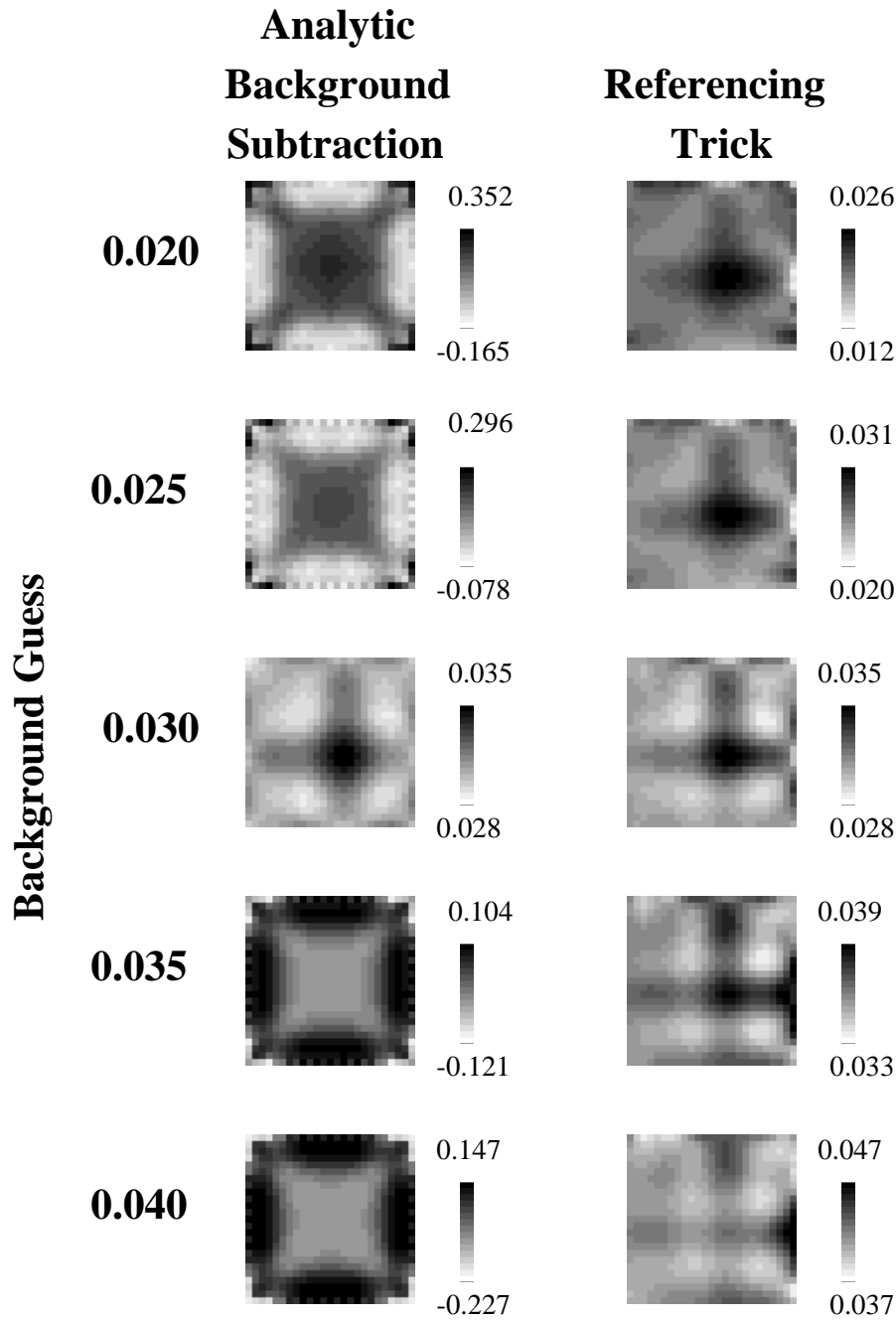
Figure 4.10: Reconstructions of absorption when the background absorption is mis-estimated. The left column of reconstruction use a single source and detector, the right uses the two source referencing method. 1000 SIRT iterations were performed with no constraints on the reconstructed absorption.
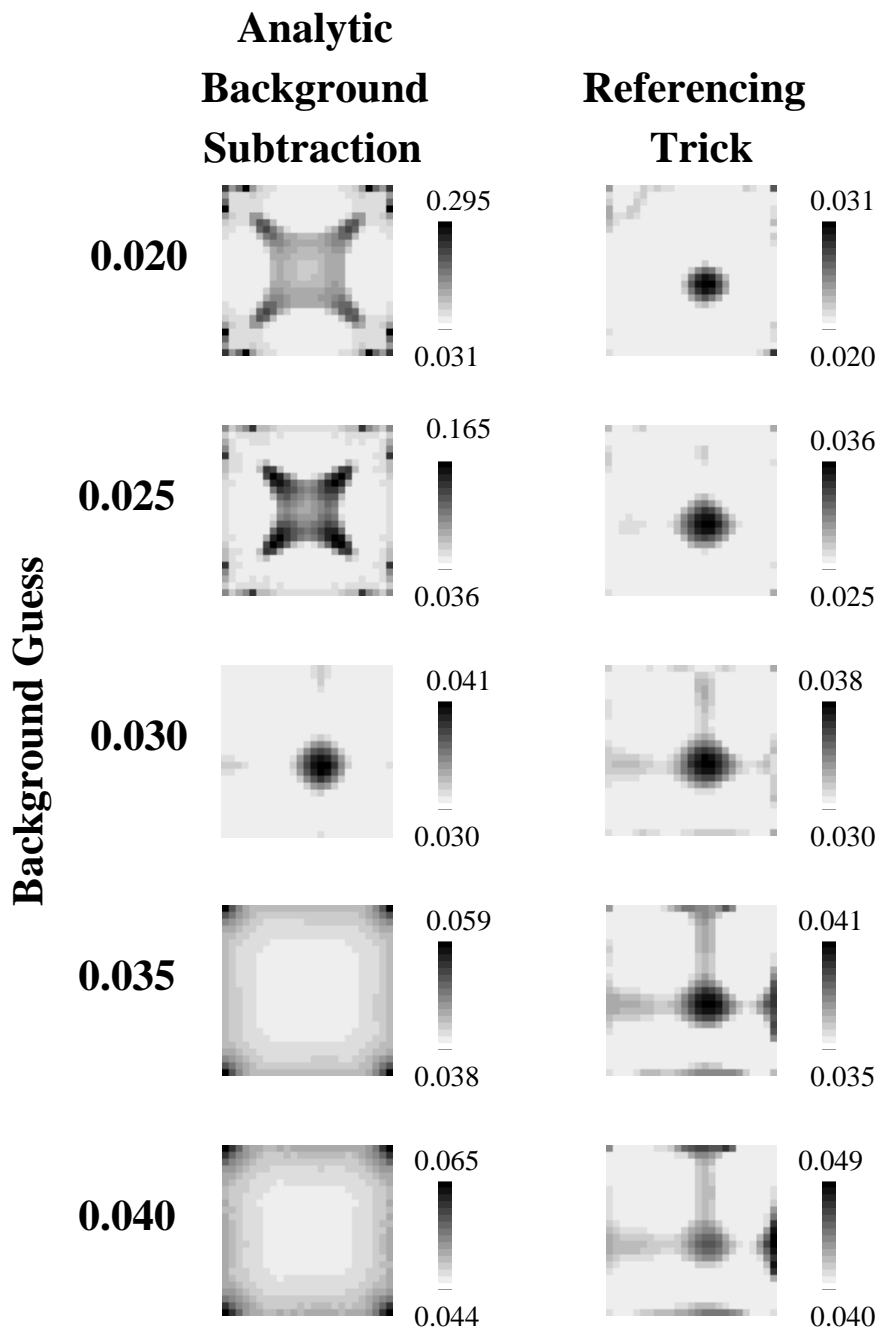
Figure 4.11: Reconstructions of absorption when the background absorption is mis-estimated. The left column of reconstruction use a single source and detector, the right uses the two source referencing method. 1000 SIRT iterations were performed with a positivity constraint on the reconstructed absorption.

must be subtracted using a theoretical model. Alternatively, investigators attempt to make measurements before and after the addition of the heterogeneity. This allows an explicit measurement of the background signal.

4.9   Experimental and Computational Results

The following experiments were performed in an effectively infinite medium using the equipment described in Chapter 3. Since at this point, we were only using the Born approximation, the initial amplitude and phase of the sources were measured for calibration purposes. A perfectly absorbing sphere was submerged, and moved in a manner to simulate the source pair scanning along the sides of 6.0 cm square as shown in figure 4.12. In each measurement the detector remained opposite the source pair, at a separation of greater than 35 transport mean free paths. 120 measurements of amplitude and phase were made around the square. The volume of the imaged region was $5 \times 5 \times 1$ cm^3.

Figure 4.12 demonstrates the reconstruction of a single perfectly absorbing spherical object (1.2 cm in diameter) from *experimental data*. The background media has $\mu_a = 0.023$ cm^{-1} and $\mu_s' = 6.0$ cm^{-1}. In this reconstruction, 1000 SIRT iterations were performed. As we start the reconstruction, the image shows a large object with a low absorption. The position is correct. Had we continued to iterate, the object would rapidly become smaller and more absorbing. We have chosen to stop iterating when the percent error between the forward model and the measured data is less than 1%.

To confirm that we are sensitive to the optical properties of the medium, a series of experiments were undertaken in which spheres of varying absorption were imaged separately using matrix inversion (SVD). The spheres were made of casting resin with titanium oxide (TiO$_2$) for scatterers and a near infrared absorbing dye for absorption [55]. The reconstructed images are shown in figure 4.13. The reconstructed $\delta\mu_a(\mathbf{r})$ for this series of experimental data is also shown in figure 4.13. Note that the reconstructed absorption (solid circles) qualitatively follows the actual object ab-
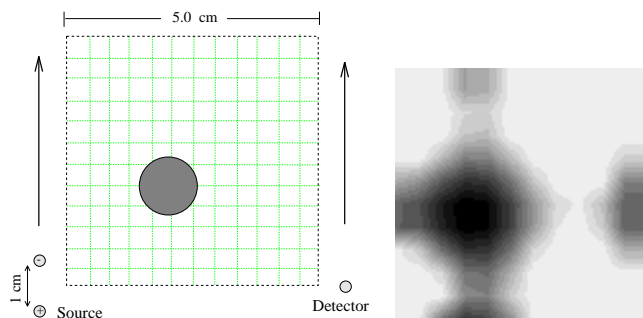
Figure 4.12: (A) The experimental setup. (B) The reconstruction of a single spherical object (1.2 cm in diameter) from experimental data. The background media has $\mu_a^o = 0.023$ cm^{-1} and $\mu_s^{o'} = 6.0$ cm^{-1}. The reconstruction was generated using 1000 SIRT iterations. The black corresponds to an absorption of 0.25 cm^{-1} and the light gray corresponds to an absorption of 0.023 cm^{-1}

sorption, but saturates at large absorption where Born approximation is expected to break down. The theoretical data created from the exact solution (solid line) show the same trend. In calculation of the forward model, we assumed that the index of refraction was homogeneous. In fact the index of refraction of the resin is 1.56 and the index of refraction of water is 1.33. This index mismatch will increase the reconstructed value of μ_a, and begins to explain the discrepancy between the true μ_a and the reconstructed value.

4.10 Updating the Weight Functions

We have seen that the inverse problem saturates for highly absorbing objects. This saturation is due to a breakdown of the Born and Rytov approximations. We can reduce this saturation effect by correcting our forward model. For example, in the Born expansion we had the equation,

$$U_{sc}(\mathbf{r}_d, \mathbf{r}_s) = -\int O(\mathbf{r})G(\mathbf{r} - \mathbf{r}_d)(U_o(\mathbf{r}, \mathbf{r}_s) + U_{sc}(\mathbf{r}, \mathbf{r}_s)), \tag{4.71}$$

and we made the approximation

$$U_o(\mathbf{r}, \mathbf{r}_s) >> U_{sc}(\mathbf{r}, \mathbf{r}_s). \tag{4.72}$$
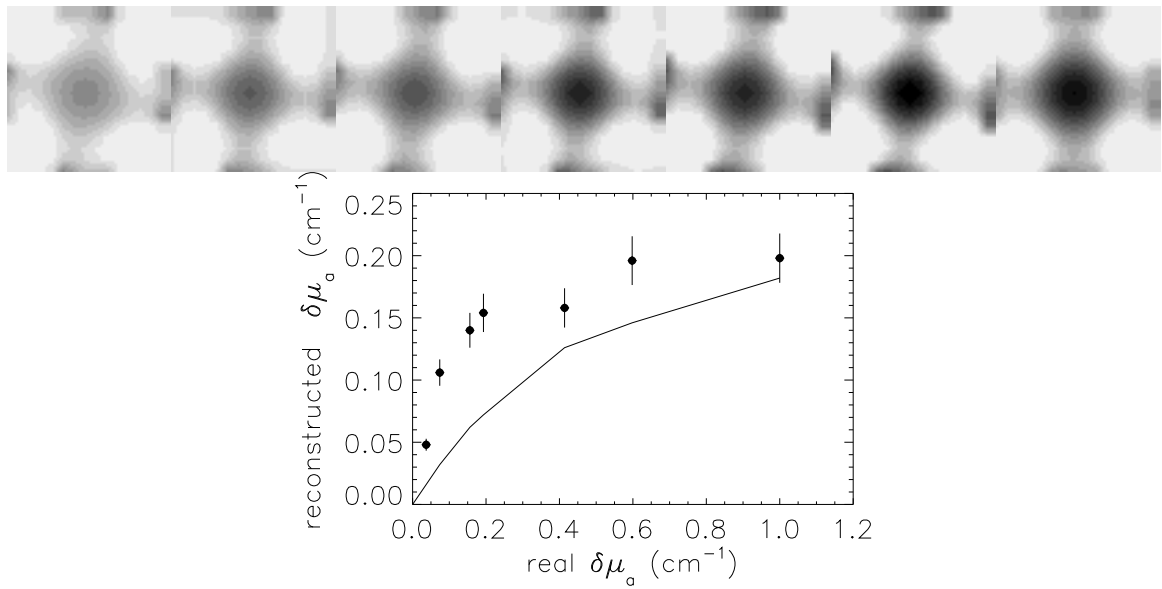
Figure 4.13: Top: In this experiment, resin spheres (1.2 cm diameter) made with a mixture of scatterer and a known concentration of ink were imaged using matrix inversion (SVD). Bottom: The reconstructed absorption from both the experimental data (circles) and the simulated data (line) are plotted vs the actual absorption. See text for further discussion. Error bars are derived from estimated the calibration errors which we believe to be most significant.

Recall that U_{sc} is the part of the DPDW which has been scattered from the heterogeneity. If we approximate U_{sc} instead of dropping it, we can improve our reconstructions. We need a heterogeneous model to approximate U_{sc}. Such models include Monte-Carlo simulations, finite difference calculations, and analytic solutions for specific geometries.

To demonstrate the procedure for improving the weights, we first look at the integral equation. Instead of approximating

$$U_{sc}(\mathbf{r}_d, \mathbf{r}_s) = -\int O(\mathbf{r})G(\mathbf{r} - \mathbf{r}_d)(U_o(\mathbf{r}, \mathbf{r}_s) + U_{sc}(\mathbf{r}, \mathbf{r}_s))d^3r, \qquad (4.73)$$

as

$$U_{sc}(\mathbf{r}_d, \mathbf{r}_s) = -\int O(\mathbf{r})G(\mathbf{r} - \mathbf{r}_d)U_o(\mathbf{r}, \mathbf{r}_s)d^3r, \qquad (4.74)$$

we use and iterative procedure,

$$U_{sc}^{n+1}(\mathbf{r}_d, \mathbf{r}_s) = -\int O(\mathbf{r})G(\mathbf{r} - \mathbf{r}_d)(U_o(\mathbf{r}, \mathbf{r}_s) + U_{sc}^n(\mathbf{r}, \mathbf{r}_s))d^3r. \qquad (4.75)$$

This procedure updates the weights in the matrix equation. We start by making a guess that there is only the homogeneous background absorption (0th order). In this case there is not heterogeneity and $U_{sc}^0 = 0$. The weights in the Born approximation are

$$W_{ij}^B \propto G(\mathbf{r}_j - \mathbf{r}_{di})U_o(\mathbf{r}_j, \mathbf{r}_{sj}). \qquad (4.76)$$

We then use the measured data to reconstruct the object. We use the results of this 0th order reconstruction, and use a heterogeneous forward model to calculate $U_o + U_{sc}^1$. Next we use U_{sc}^1 as an approximation to generate a new set of weights, i.e.,

$$W_{ij}^B \propto G(\mathbf{r}_j - \mathbf{r}_{di})(U_o(\mathbf{r}_j, \mathbf{r}_{sj}) + U_{sc}^1(\mathbf{r}_j, \mathbf{r}_{sj})). \qquad (4.77)$$

We will show the results of this weight updating routing in section 4.12 using an analytic solution for a spherical inhomogeneity.

We have updated the weights using a heterogeneous model for photon propagation. One could use the Born or Rytov formulations for the scattered wave in the

heterogeneous forward model. This is certainly possible, but there is a small subtlety. To calculate the scattered wave at a particular voxel k, from a source i, one must calculate the sum (in the Born approximation),

$$U_{sc}(\mathbf{r}_k, r_{si}) = \sum_j U_o(\mathbf{r}_j, \mathbf{r}_{si}) G(\mathbf{r}_k - \mathbf{r}_j) h^3 / D. \tag{4.78}$$

$$G(\mathbf{r}_k - \mathbf{r}_j) = \frac{\exp(|\mathbf{r}_k - \mathbf{r}_j|)}{4\pi |\mathbf{r}_k - \mathbf{r}_j|} \tag{4.79}$$

We cannot calculate this when $j = k$. This is the so called 'self-interaction term'. Jacques *et al.* [56] have calculated the value of the self interaction term and incorporated into a forward model called the 'system of virtual sources' (SVS). The SVS model has been incorporated into the PMI code (see chapter E) and will be released in a future version.

We have assumed throughout this discussion that we were using a good value for the background properties of absorption and scattering. If the system is totally unknown, one would like to update the background values to improve the image.

4.11 Resolving Multiple Objects

Figure 4.14 demonstrates that we are able to resolve multiple absorbing objects. The left panels (a-b) show the reconstruction of two 1.0 cm diameter perfectly absorbing spheres from experimental data. The top (a) is the reconstruction using singular value decomposition and analysis, and the bottom (b) panel is a reconstruction using 3000 iterations of SIRT.

We have also investigated the effect of modulation frequency on resolution of multiple objects using simulated data derived from the analytic solution to the diffusion equation for a sphere embedded in an otherwise homogeneous medium [10]. Panels (c-f) are images of two perfectly absorbing spheres from simulated data using a different sphere configuration. In panels (c-d) (background $\mu_a = 0.1$ cm^{-1}, inside the spheres $\mu_a = 0.4$ cm^{-1}), we see an increase in image quality as the modulation frequency is increased from 50 MHz (c) to 1 GHz (d). However, when the background

absorption is high (background $\mu_a = 1.0$ cm^{-1}, inside the spheres $\mu_a = 4.0$ cm^{-1}), the image quality does not noticeably improve as the modulation frequency is increased from 50 MHz (e) to 1 GHz (f). This may be understood qualitatively by noting that the wavenumber of a DPDW,

$$k = \sqrt{(-v\mu_a + i\omega)/D}, \qquad (4.80)$$

is nearly independent of ω when $v\mu_a >> \omega$. This result suggests that sources at low modulation frequencies and sources with high frequency components will yield roughly equivalent images in media characterized by a high average absorption such as the brain. On the other hand, when imaging within bodies with low average absorption, such as the breast, high modulation frequency images will give better resolution.

4.12   DPDW Imaging Combined With Other Imaging Modalities

An important contribution of the optical method is its ability to quantify the concentrations of physiologically important pigments, such as oxygenated and de-oxygenated hemoglobin, by providing absolute spatial quantification of scattering and absorption coefficients in the near infra-red region. Anatomical details derived from a conventional medical image, as in the case of X-ray tomography or MRI, can be taken into account in order to improve the quantitative accuracy of the optical image. The feasibility of simultaneously combining optical with other imaging modalities promises to increase the diagnostic certainty of the acquired images. Other researchers have used a priori structural information to improve the formulation of the forward problem [57, 58]. In this section we describe an algorithm which uses structural information to reduce the number of unknowns in the inverse problem, from the number of voxels in the image, to the number of tissue types. This reduces both the complexity of the inverse problem and the number of measurements necessary for an accurate reconstruction. We present simulations which confirm the efficiency of the algorithm, and experimental measurements on a tissue phantom which demonstrate the feasibility of
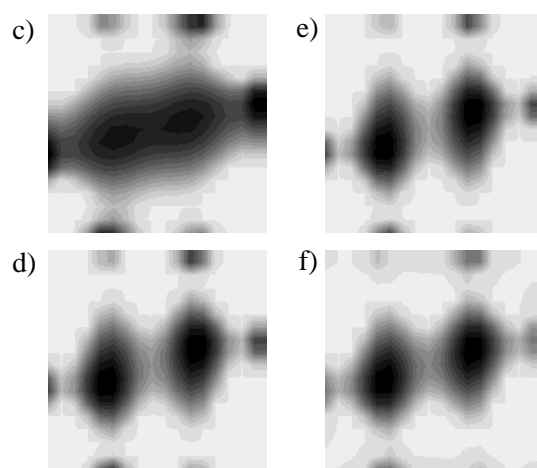
Experimental Data
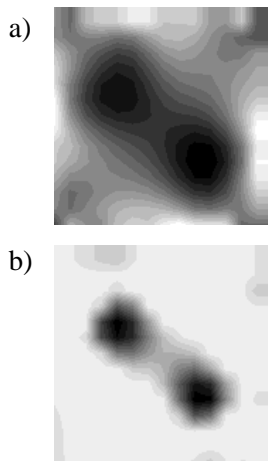
Simulated Data

Figure 4.14: The left panels (a-b) show the reconstruction of two 1.0 cm diameter perfectly absorbing spheres from experimental data. The top (a) is the reconstruction using singular value decomposition and analysis, and the bottom (b) panel is a reconstruction using 3000 iterations of SIRT. Panels (c-f) are images of two perfectly spheres from simulated data using a different sphere configuration. In panels (c-d) (background $\mu_a = 0.1$ cm^{-1}, inside the spheres $\mu_a = 0.4$ cm^{-1}), we see an increase in image quality as the modulation frequency is increased from 50 MHz (c) to 1 GHz (d). However, when the background absorption is high (background $\mu_a = 1.0$ cm^{-1}, inside the spheres $\mu_a = 4.0$ cm^{-1}) the image quality does not noticeably improve as the modulation frequency is increased from 50 MHz (e) to 1 GHz (f).

fat 1	fat 2	fat 3
fat 4	fat 5	fat 6
vein 7	tumor 8	tumor 9

Figure 4.15: A simple breast model. This over-simplified model is used for describing the matrix reduction algorithm.

the method to be applied in a real system.

Let us consider an absorbing inhomogeneity embedded in a region broken into n voxels. For simplicity we assume n=9 as depicted in figure 4.15.

Thus we have one unknown value of $\delta\mu_a$ in each of the nine voxels. We make one measurement of the amplitude and phase of the diffuse photon density wave, from which we can calculate the real and imaginary part of the scattered phase (ϕ_{sc}) using the Rytov solution. The scattered phase will obey the following matrix equation:

$$\begin{pmatrix} \Re[\phi_{sc}(\mathbf{r}_s,\mathbf{r}_d)] \\ \Im[\phi_{sc}(\mathbf{r}_s,\mathbf{r}_d)] \end{pmatrix} = \begin{pmatrix} \Re[W_{11}] & \ldots & \Re[W_{19}] \\ \Im[W_{11}] & \ldots & \Im[W_{19}] \end{pmatrix} \cdot \begin{pmatrix} \delta\mu_a^1 \\ \vdots \\ \delta\mu_a^9 \end{pmatrix} \qquad (4.81)$$

Here $\delta\mu_a^i$ is the absorption in the ith voxel. If the structural information is known and we assume that each component in the structure has uniform optical properties, then the problem dramatically simplifies. We need only to solve for the absorption coefficients of each *type* of inhomogeneity. For example, if the sample is composed of fat (background), vein and tumor, then we only have two actual unknowns, (since

the perturbation to the background, fat, is zero). We may then rewrite:

$$\begin{pmatrix} \Re[\phi_{sc}(\mathbf{r}_s, \mathbf{r}_d)] \\ \Im[\phi_{sc}(\mathbf{r}_s, \mathbf{r}_d)] \end{pmatrix} = \begin{pmatrix} \Re[W_{11}] & \vdots & \Re[W_{19}] \\ \Im[W_{11}] & \vdots & \Im[W_{19}] \end{pmatrix} \cdot \begin{pmatrix} \delta\mu_a^{fat1} = 0 \\ \delta\mu_a^{fat2} = 0 \\ \delta\mu_a^{fat3} = 0 \\ \delta\mu_a^{fat4} = 0 \\ \delta\mu_a^{fat5} = 0 \\ \delta\mu_a^{fat6} = 0 \\ \delta\mu_a^{vein7} \\ \delta\mu_a^{tumor8} \\ \delta\mu_a^{tumor9} \end{pmatrix} \qquad (4.82)$$

as

$$\begin{pmatrix} \Re[\phi_{sc}(\mathbf{r}_s, \mathbf{r}_d)] \\ \Im[\phi_{sc}(\mathbf{r}_s, \mathbf{r}_d)] \end{pmatrix} = \begin{pmatrix} \Re[W_{17}] & \Re[\sum_{j=8}^{9} W_{1j}] \\ \Im[W_{17}] & \Im[\sum_{j=8}^{9} W_{19}] \end{pmatrix} \cdot \begin{pmatrix} \delta\mu_a^{vein} \\ \delta\mu_a^{tumor} \end{pmatrix} \qquad (4.83)$$

In this way we have reduced the number of linear equations to be solved, from nine to two. This algorithm is easily extended for multiple measurements. It is interesting to note that the sum of the weights in the above matrix represent our sensitivity of each measurement to each tissue type. These sums can be used to design the experimental setup and maximize sensitivity to the tissue type of interest.

Simulations were performed using PMI software [12]. A matrix inversion technique (SVD) was employed to solve for the absorption coefficient of inhomogeneities in a background medium. Because the problem has been dramatically simplified, there was no need for any regularization or singular value analysis. 1% amplitude and 0.5 degree phase noise was added to all simulated data. In all of the following simulations the optical properties of the background were $\delta\mu_a = 0.03$ cm^{-1} and $\mu_s' = 10.0$ cm^{-1} and the source-detector separation was 6 cm.

We first tested this algorithm on a series of simple one object systems. The 1 cm diameter spheres had the same scattering properties as the surrounding medium, but the absorption varied from 0.035 to 0.355 cm^{-1}. The area of interest, a 6 cm x 6 cm x 1 cm region, was divided into 120 x 120 x 20 = 288,000 voxels. Using a single source-detector pair and making measurements of amplitude and phase at 4 different source modulation frequencies (50, 200, 350, 500 Mhz), we had a 8 x 288,000 matrix to invert. But using the a priori structural information we were able to compress the 8 x 288,000 matrix down to a 8 x 1 matrix. In this reconstruction the computation time was totally dominated by the time it takes to calculate the weights, and the matrix inversion time was negligible. In figure 4.16 the reconstructed value of the object absorption is plotted versus the true value for each sphere simulation (labeled 1st iteration). Note that the reconstructed values agree well at low absorption, but show saturation effects at higher absorption.

As we mentioned earlier, these saturation effects are a result of the breakdown of the Rytov approximation. Basically, we have used a homogeneous model to calculate the weight functions. To improve the reconstructions, we must take into account that there is a heterogeneity present. When we updated the weight functions using the 1st iteration results, as suggested by Pogue et al. [20], we were able to overcome the saturation effects. The imaging process now consists of several steps;

1. Create the weights using a homogeneous model.

2. Calculate the inverse using SVD.

3. Use this solution to calculate the weights using a heterogeneous model.

4. Calculate the inverse using SVD.

We have used the exact solution for a sphere to calculate the heterogeneous weights. The results of this iterative process are also shown in 4.16, labeled 2nd iteration.

The next simulation used six objects in the medium (background) as shown in Fig. 3. Objects a,b,c,d had μ_a =0.036 cm^{-1}, object e had μ_a =0.042 cm-1 and object f had μ_a =0.050 cm^{-1}. A single source and detector were scanned along the sides of
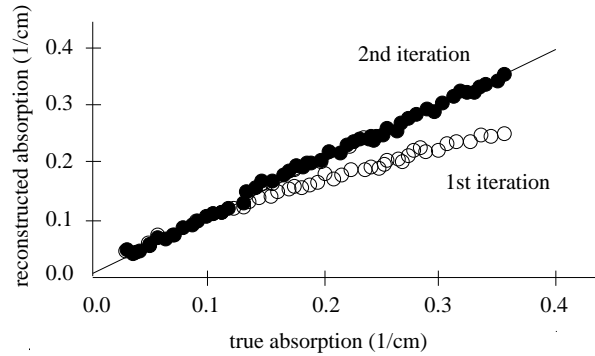
Figure 4.16: 1st and 2nd iteration of reconstructed absorption versus the true value, for a single spherical inhomogeneity.
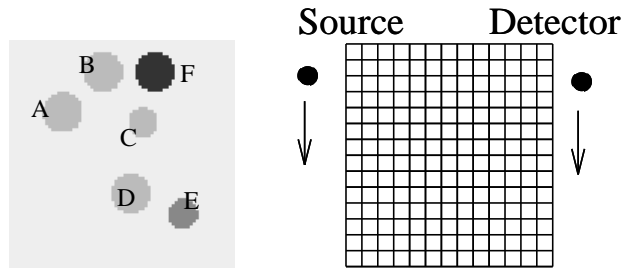

Figure 4.17: Simulation with six absorbing inhomogeneities. Since the size and position of the spheres are known, the 'reconstructed' image will look just like the original image.

the square. Measurements were simulated at three modulation frequencies (0, 250, 500 Mhz) and 14 source-detector positions. When given the position of the objects the algorithm reconstructs accurately the absorption coefficients as shown in Table 4.1.

Finally, a tissue phantom was built, with a geometry resembling a compressed breast as shown in figure 4.18. The phantom was made from clear polyester resin, in which titanium oxide particles were suspended to create a highly scattering medium (as described by Firbank *et al.* [55]). Quantities of the scatterer and India ink were added to give an absorption coefficient μ_a=0.028 cm^{-1} and a reduced scattering coefficient 6.5 cm^{-1} (780 nm), values which are close to the values measured for the human breast tissue [22]. The optical properties of the model were verified by inde-

Sphere	Real μ_a (cm^{-1})	Recon. μ_a (cm^{-1})
a, b, c, d	0.036	0.037
e	0.042	0.045
f	0.050	0.056

Table 4.1: Reconstruction results for multiple absorbing inhomogeneities.

pendent time-resolved spectroscopy (TRS) measurements (see appendix B for a brief overview of the TRS device). A two source one detector configuration was used as depicted in Fig. 5b. The sources were multiplexed (DiCon Fiber Optics multichannel fiber optic switch). In all measurements a 780 nm laser source was employed. In order to create an inhomogeneity, a 12 mm diameter, 35 mm long cylinder was drilled in the phantom. The volume was filled sequentially with twelve different solutes of intralipid and india ink. The concentration of dye was altered in precalculated steps to give absorption values in the range 0.02 - 0.2 cm^{-1}. A TRS system based on the time-correlated single photon counting was used for the measurements.

As we discussed in section 4.8, we must divide out the homogeneous signal to solve for the scattered phase. In the previous computer simulations, we were able to divide out the homogeneous signal using and analytic solution. However in the experimental system, we were not able to obtain such a measurement. To eliminate the homogeneous signal, we used the referencing scheme discussed previously. Briefly, this scheme involves comparing two measurements with equal source-detector separations to eliminate the background contribution. For each intralipid-dye solution a single pair of measurements was acquired. The time resolved data were transformed into the frequency domain using the FFT, and six frequencies, all below 500MHz, were selected. The algorithm reduced a 6 x 144,000 matrix down to a 6 x 1 matrix. (Since only one absorbing inhomogeneity was present to the phantom, the algorithm had to solve only for one unknown value). Figure 4.18 shows the reconstructed absorption
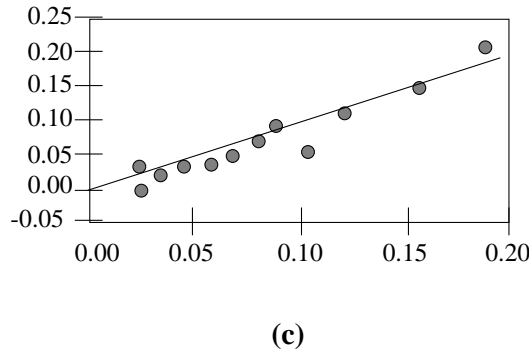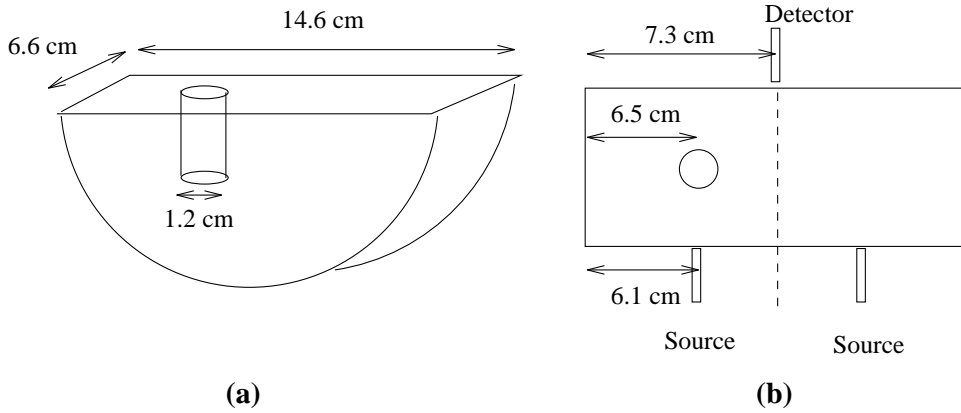
(a)

(b)

(c)

Figure 4.18: A tissue phantom simulating a human breast with one heterogeneity. D denotes the detector and S the sources. (a) Side view, (b) top view. (c) The results from the inversion. See text for more discussion.

values, after one iteration, in comparison with the theoretically calculated ones.

The algorithm we present here simplifies the calculation load by reducing the number of unknowns to the number of regions with different optical properties. These results clearly demonstrate that given the geometry we can accurately reconstruct the absorption of the different regions of the various models. In the case of MRI-guided optical tomography of the human breast, boundary conditions and inhomogeneous background regions are expected to affect the accuracy of the reconstruction. Still we believe that such a method will eventually prove to be of clinical value.

4.13   Finite Systems

In our lab, we have inverted an approximate solution to the infinite, heterogeneous diffusion equation. We realize that in clinical situations, we will not have an infinite system, but rather a system with irregular boundaries. Although we have not investigated finite systems in this work, many investigators have studied how to handle boundary conditions for homogeneous, finite media [59]. In this section we examine the general problem, and then consider the simple, yet clinically relevant geometry of the semi-infinite system.

The most general goal is to write down a solution for the photon density in a homogeneous volume enclosed by a surface, S. We will use the same formalism as the solution of the electrostatic boundary-value problem using Green functions. Using Green's theorem, for a source distribution $A(\mathbf{r})$,

$$U(\mathbf{r}) = \int_V A(\mathbf{r}')G(\mathbf{r},\mathbf{r}')d^3r' + \frac{1}{4\pi}\int_S \left[G(\mathbf{r},\mathbf{r}')\frac{\partial U}{\partial n'} - U(\mathbf{r}')\frac{\partial G}{\partial n'}\right]d^2r'. \qquad (4.84)$$

In the heterogeneous absorption case $A(\mathbf{r}) = U_o(\mathbf{r},\mathbf{r}_s)v\delta\mu_a(\mathbf{r})/D$.

Investigators have used Monte Carlo simulations and experimental results to show that the true boundary conditions for the case of finite media are well modeled by the extrapolated zero boundary condition [60, 61, 62, 63]. The extrapolated zero boundary condition asserts that the photon density is zero a distance of $0.704l^*$ from the actual (planar) boundary [64]. Thus, we re-draw the boundaries at the extrapolated position, and use the condition that $U = 0$ on the extrapolated surface. Equation 4.84 becomes,

$$U(\mathbf{r}) = \int_V A(\mathbf{r}')G(\mathbf{r},\mathbf{r}')d^3r' + \frac{1}{4\pi}\int_S G(\mathbf{r},\mathbf{r}')\frac{\partial U}{\partial n'}da'. \qquad (4.85)$$

This general equation may be simplified by choosing a Green function that satisfies Dirichlet boundary conditions (i.e. $G = 0$ on the extrapolated surface). Then

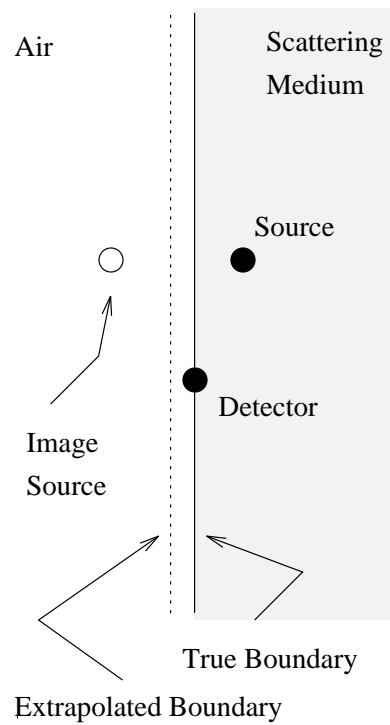$$U(\mathbf{r}) = \int_V A(\mathbf{r}')G(\mathbf{r},\mathbf{r}')d^3r' \qquad (4.86)$$

Figure 4.19: An extrapolated zero boundary is a good approximation for the photon density boundary conditions in the semi-infinite case. Here er see how a source on the boundary is transformed using a true source position and an image source centered about the extrapolated boundary.

Arridge *et al.* [59] have worked out the Green function solutions for Dirichlet boundary conditions for a variety of different homogeneous finite systems such as semi-infinite, slab, spherical and cylindrical geometries. It is also possible to use other methods such as Monte-Carlo and Finite Element to derive the Green function solutions.

For the semi-infinite case, we can use the method of images to find the Green function which obeys the Dirichlet boundary conditions (see figure 4.19). In this case

$$G(\mathbf{r}, \mathbf{r}') = \frac{\exp(ik|\mathbf{r} - \mathbf{r}'|)}{4\pi|\mathbf{r} - \mathbf{r}'|} - \frac{\exp(ik|\mathbf{r} - \mathbf{r}_i|)}{4\pi|\mathbf{r} - \mathbf{r}_i|} \qquad (4.87)$$

where $\mathbf{r}'$ is the position of the source in the sample volume, and $\mathbf{r}_i$ is the position of the image source located on the other side of the extrapolated boundary. Using this Green function we can now calculate the incident DPDW,

$$U(\mathbf{r}, \mathbf{r}_s) = \frac{B}{D}\frac{\exp(ik|\mathbf{r} - \mathbf{r}_s|)}{4\pi|\mathbf{r} - \mathbf{r}_s|} - \frac{B}{D}\frac{\exp(ik|\mathbf{r} - \mathbf{r}_i|)}{4\pi|\mathbf{r} - \mathbf{r}_i|} \qquad (4.88)$$

$$= U_o(\mathbf{r}, \mathbf{r}_s) - U_o(\mathbf{r}, \mathbf{r}_i). \qquad (4.89)$$

where $\mathbf{r}_s$ is the position of the source in the sample volume, and $\mathbf{r}_i$ is the image of $\mathbf{r}_s$.

We now plug the incident DPDW solution and the Green Function solution for the finite system into the weights (equation 4.13,4.26). For example, in the Born approximation, for a detector at $\mathbf{r}_d$, equation 4.13 becomes

$$U_{sc}(\mathbf{r}_d, \mathbf{r}_s, \mathbf{r}_i) = -\int d^3r \underbrace{G(\mathbf{r}_d - \mathbf{r})}_{semi-infinite} O(\mathbf{r}) \underbrace{U_o(\mathbf{r}, \mathbf{r}_s)}_{semi-infinite} \qquad (4.90)$$

$$= -\int d^3r \left[G(\mathbf{r}_d, \mathbf{r}) - G(\mathbf{r}_d, \mathbf{r}')\right] \qquad (4.91)$$

$$\times O(\mathbf{r})\left[U_o(\mathbf{r}, \mathbf{r}_s) - U_o(\mathbf{r}, \mathbf{r}_i)\right]$$

where $\mathbf{r}'$ is the image voxel position.

Multiple image sources can be used to solve for the scattered wave in the case of the slab, the cube and other planar geometries. For curved geometries one has to take more care in defining the extrapolated surface.